

# Salt-Assisted Low-Temperature Growth of 2D Bi<sub>2</sub>O<sub>2</sub>Se with Controlled Thickness for Electronics

Usman Khan,\* Adeela Nairan, Karim Khan, Sean Li, Bilu Liu, and Junkuo Gao\*

Bi<sub>2</sub>O<sub>2</sub>Se is the most promising 2D material due to its semiconducting feature and high mobility, making it propitious channel material for high-performance electronics that demands highly crystalline Bi<sub>2</sub>O<sub>2</sub>Se at low-growth temperature. Here, a low-temperature salt-assisted chemical vapor deposition approach for growing single-domain Bi<sub>2</sub>O<sub>2</sub>Se on a millimeter scale with thicknesses of multilayer to monolayer is presented. Because of the advantage of thickness-dependent growth, systematical scrutiny of layer-dependent Raman spectroscopy of Bi<sub>2</sub>O<sub>2</sub>Se from monolayer to bulk is investigated, revealing a redshift of the A<sub>1g</sub> mode at 162.4 cm<sup>-1</sup>. Moreover, the long-term environmental stability of ≈2.4 nm thick Bi<sub>2</sub>O<sub>2</sub>Se is confirmed after exposing the sample for 1.5 years to air. The backgated field effect transistor (FET) based on a few-layered Bi<sub>2</sub>O<sub>2</sub>Se flake represents decent carrier mobility (≈287 cm<sup>2</sup> V<sup>-1</sup> s<sup>-1</sup>) and an ON/OFF ratio of up to 10<sup>7</sup>. This report indicates a technique to grow large-domain thickness controlled Bi<sub>2</sub>O<sub>2</sub>Se single crystals for electronics.

flexibility, outperformed electrical, optical, thermoelectric, and electrochemical characteristics, and compatibility with other materials.<sup>[1–13]</sup> In the past few years, 2D materials have been employed for the state-of-the-art electronic and optoelectronic devices.<sup>[14–18]</sup> Among the broad list of reported 2D materials, graphene is the most-prominent material due to its remarkably high carrier mobility.<sup>[19]</sup> However, the on/off switching in graphene-based field-effect transistors (FETs) is immensely difficult due to its zero-bandgap. 2D black phosphorous and 2D perovskite are mostly unstable in the air, and the growth of these materials is onerous by traditional chemical vapor deposition (CVD), restricting their widespread electronic applications.<sup>[20–22]</sup> As an alternative, 2D transition metal dichalcogenides

## 1. Introduction

The rise of 2D materials has garnered considerable interest caused of their planar structures, free of dangling bonds, layer-dependent electronic band structure, excellent mechanical

(TMDCs) are suitable candidates for high-performance optoelectronics attributable to the layer-dependent optical absorption; however, the low-carrier mobility of these materials hinders their execution in electronics.<sup>[23,24]</sup> It is, therefore, necessary to explore an air-stable 2D material with suitable bandgap and high carrier mobility for electronic and optoelectronic applications.

During the last half-decennium, Bismuth oxyselenide (Bi<sub>2</sub>O<sub>2</sub>Se) FETs have been devoted great attention due to their low subthreshold swing (≈65 mV dec<sup>-1</sup>) and high low-temperature mobility (> 20k cm<sup>2</sup> V<sup>-1</sup> s<sup>-1</sup> at 2 K).<sup>[25]</sup> The moderate bandgap (≈0.8 eV) and competent light absorption make Bi<sub>2</sub>O<sub>2</sub>Se an opportune semiconducting material for electronic applications.<sup>[26–31]</sup> In order to achieve Bi<sub>2</sub>O<sub>2</sub>Se-based FETs, the acquisition of large-sized atomically thin 2D material is of considerable significance. So far, 2D Bi<sub>2</sub>O<sub>2</sub>Se has been synthesized by various techniques, including molecular beam epitaxy (MBE),<sup>[32]</sup> pulsed laser deposition (PLD),<sup>[33]</sup> wet-chemical methods,<sup>[34–37]</sup> physical vapor deposition (PVD),<sup>[30]</sup> and CVD method.<sup>[25,28,38–43]</sup> Among these growth strategies, Bi<sub>2</sub>O<sub>2</sub>Se attained by PLD or MBE requires expensive equipment and ultra-high vacuum. Currently, the large size and crystal quality of material synthesized with the wet-chemical method are huge challenges. The growth of millimeter-sized Bi<sub>2</sub>O<sub>2</sub>Se has been investigated at a high temperature of 700 °C using the PVD method, which may limit its application for temperature-sensitive substrates. Compared with the aforementioned methods, CVD is the preferred technique to produce Bi<sub>2</sub>O<sub>2</sub>Se; however, the domain size of 2D Bi<sub>2</sub>O<sub>2</sub>Se flakes is only a few hundreds of micrometers.<sup>[25,28,39,41]</sup> It is obvious that the controlled growth

U. Khan, A. Nairan, J. Gao  
Institute of Functional Porous Materials  
School of Materials Science and Engineering  
Zhejiang Sci-Tech University  
Hangzhou 310018, P. R. China  
E-mail: usmankhan.2017@tsinghua.org.cn; jkgao@zstu.edu.cn

U. Khan, A. Nairan, J. Gao  
Zhejiang Provincial Innovation Center of Advanced Textile Technology  
Shaoxing 312000, P. R. China

K. Khan  
School of Electrical Engineering & Intelligentization  
Dongguan University of Technology  
Dongguan 523808, P. R. China

S. Li  
School of Materials Science and Engineering  
The University of New South Wales  
Sydney 2052, Australia

B. Liu  
Shenzhen Geim Graphene Center  
Tsinghua-Berkeley Shenzhen Institute & Institute of Materials Research  
Tsinghua Shenzhen International Graduate School  
Tsinghua University  
Shenzhen 518055, P. R. China

 The ORCID identification number(s) for the author(s) of this article can be found under <https://doi.org/10.1002/smll.202206648>.

DOI: 10.1002/smll.202206648

of large-sized 2D Bi<sub>2</sub>O<sub>2</sub>Se at relatively low temperature is still at an early stage.

Due to their advantages, salts have been widely exerted to synthesize carbon nanostructures, oxide ceramic powders, and TMDCs in recent years.<sup>[44–50]</sup> First, the strong polarizing forces of salts destabilize the covalent, metallic, and ionic bonds.<sup>[51]</sup> Second, the growth products can be isolated because of the high water solubility of salts after immersing the products in water and filtering the products with the aid of filter membranes.<sup>[51]</sup> Third, salts have the ability to enhance the mass flux by decreasing the melting points of precursors to form oxychlorides to increase the reaction rate.<sup>[52]</sup> Therefore, water-soluble salts such as KBr and NaCl, which are abundant in nature and thermally stable,<sup>[53]</sup> dawn as an essential additive in traditional CVD procedures to grow 2D materials. The involvement of salts in low-dimensional materials can be categorized into two types. In the molten-salt-assisted method, they can be mixed with reactants as a promoter/additives. They serve as a growth substrate to facilitate the production of nanomaterials in the salt-template-directed technique. In the former case, the mixture of metallic precursors and salts introduces active intermediates at relatively low evaporation temperatures to enhance the metallic precursor's supply, thereby contributing enough nucleation sites on the growth substrate.<sup>[54]</sup> In the latter case, salts are used as a substrate to promote the growth of nanomaterials by considering the excellent thermal stability and high surface area.<sup>[53]</sup>

Inspired by the above achievement, we report an efficient salt-assisted CVD strategy for the low-temperature growth of atomically thin high-quality 2D Bi<sub>2</sub>O<sub>2</sub>Se with a controllable thickness. The average domain size of Bi<sub>2</sub>O<sub>2</sub>Se is ≈1.3 mm, which is the largest domain size of a single crystal flake ever reported through the CVD method so far. The thickness and domain size of Bi<sub>2</sub>O<sub>2</sub>Se can be precisely controlled by modifying the molar ratio of precursors and the growth temperature. Layer-dependent Raman spectroscopy is investigated by taking advantage of the tunable thickness of salt-assisted grown Bi<sub>2</sub>O<sub>2</sub>Se. We observe a redshift of ≈5.7 cm<sup>-1</sup> for the out-of-plane vibrational mode A<sub>1g</sub> of monolayer Bi<sub>2</sub>O<sub>2</sub>Se with an increase in thickness. Most importantly, the A<sub>1g</sub> vibrational mode is absent in monolayer to trilayer Bi<sub>2</sub>O<sub>2</sub>Se, which can be used for thickness determination. The stability of Bi<sub>2</sub>O<sub>2</sub>Se after air exposure for 1.5 years demonstrates an immaculate surface with excellent crystallinity in the ambient environment. Furthermore, a few-layer Bi<sub>2</sub>O<sub>2</sub>Se-based FET represents an excellent high on/off ratio of ≈10<sup>7</sup> and mobility of ≈287 cm<sup>2</sup> V<sup>-1</sup> s<sup>-1</sup>, which displays its possibility for advanced manufacturing technology.

## 2. Results and Discussion

Instigated by the triumph of salt-assisted CVD techniques for synthesizing 2D TMDCs and non-layered materials, we successfully grow atomically thin 2D Bi<sub>2</sub>O<sub>2</sub>Se flakes using Bi<sub>2</sub>Se<sub>3</sub>.<sup>[52,55,56]</sup> To analyze the thermal stability of Bi<sub>2</sub>Se<sub>3</sub>, thermogravimetric analysis (TGA) was carried out from room temperature to 1000 °C, and its weight loss curve is shown in Figure S1 (Supporting Information). The incorporation of salt can lower the high melting point of Bi<sub>2</sub>Se<sub>3</sub> (≈710 °C)<sup>[57,58]</sup> and hence support the reaction to grow 2D Bi<sub>2</sub>O<sub>2</sub>Se. A schematic

illustration for growing 2D Bi<sub>2</sub>O<sub>2</sub>Se flakes by a salt-assisted CVD method is represented in Figure 1a. In this work, NaCl is mixed with Bi<sub>2</sub>Se<sub>3</sub> to sever as a precursor, and NaCl plays a vital role in assisting the growth reaction. Several 1 × 1 cm<sup>2</sup> sized mica substrates were located in the tube furnace to collect the final product (see the Experimental Section for details). As shown in Figure 1b, the ultra-large irregularly shaped Bi<sub>2</sub>O<sub>2</sub>Se flake is grown on mica with a size of more than 3 mm. An atomic force microscope (AFM) image of a ≈3 mm Bi<sub>2</sub>O<sub>2</sub>Se flake, recorded at a white square area represented in Figure 1b and Figure S2(a) (Supporting Information), is depicted in Figure S2(b) (Supporting Information). The topographical analysis confirms a clean and homogeneous surface, and the thickness of the sample of ≈1.9 nm represents a trilayer flake. The XRD pattern of the Bi<sub>2</sub>O<sub>2</sub>Se nanosheet is represented in Figure S3 (Supporting Information). All the diffraction peaks are reflected from (001) planes of Bi<sub>2</sub>O<sub>2</sub>Se with crystal orientation along the *c*-axis, and the results are consistent with the literature.<sup>[59]</sup> The salt-assisted CVD technique displayed the ability to grow ultra-large single domain (≈1.3 mm) 2D Bi<sub>2</sub>O<sub>2</sub>Se flakes, as shown in Figure 1c. The thickness of ultra-large single domain Bi<sub>2</sub>O<sub>2</sub>Se flake recorded at a white square area highlighted in Figure S4(a) (Supporting Information) is shown in Figure S4(b) (Supporting Information). The thickness of the flake is ≈1.6 nm which represents a bilayered flake. It should be noted that the morphology is modified from irregular to a regular square-shaped Bi<sub>2</sub>O<sub>2</sub>Se with an appropriate quantity of NaCl. Adding NaCl can significantly reduce the melting point of Bi<sub>2</sub>Se<sub>3</sub> and guarantees a high mass flux of metallic precursor. It is worth mentioning that by optimizing the salt-to-Bi<sub>2</sub>Se<sub>3</sub> ratio, the domain sizes of the Bi<sub>2</sub>O<sub>2</sub>Se can be precisely modified to achieve ultra-large single crystalline Bi<sub>2</sub>O<sub>2</sub>Se. The largest currently reported domain sizes of single crystalline Bi<sub>2</sub>O<sub>2</sub>Se are in the range of ≈10–750 μm (Figure 1d).<sup>[25,28,30,39–41,60–62]</sup>

The crystal structure determination and quality of synthesized samples were investigated by transmission electron microscope (TEM) after transferring 2D Bi<sub>2</sub>O<sub>2</sub>Se flakes. The samples were transferred similarly to TMDCs using poly (methyl methacrylate) (PMMA) coating on Bi<sub>2</sub>O<sub>2</sub>Se/mica and then transferred onto a Cu grid, as shown in Figure 1e. The TEM image of 2D Bi<sub>2</sub>O<sub>2</sub>Se captured at high resolution demonstrates a *d*-spacing of ≈2.8 Å for the (110) plane (Figure 1f). The nature of crystal structure and quality of synthesized 2D Bi<sub>2</sub>O<sub>2</sub>Se was further elucidated with the help of a selected area electron diffraction (SAED) that represents (1 $\bar{1}$ 0), (110), and (200) bright spots, and the tetragonal structure as shown in Figure 1g. These analyses confirm the high crystal quality of Bi<sub>2</sub>O<sub>2</sub>Se flakes without the presence of other impurities such as Bi<sub>2</sub>O<sub>3</sub> or Bi<sub>2</sub>Se<sub>3</sub>. Next, we inspected the quality of salt-assisted CVD growth of Bi<sub>2</sub>O<sub>2</sub>Se flakes based on the chemical composition with X-ray photoelectron spectroscopy (XPS). The XPS survey scan of 2D Bi<sub>2</sub>O<sub>2</sub>Se is shown in Figure S5 (Supporting Information). The information on the chemical bonding states of O, Se, and Bi is displayed in Figure 1h–j. The peaks in the XPS spectrum of Bi are centered at 164 eV for Bi 4f<sub>7/2</sub> and 158.8 eV for Bi 4f<sub>5/2</sub>, which can be assigned to metallic Bi in bismuth oxide (Figure 1h). The peaks of Se are centered at 54.1 eV for Se 3d<sub>3/2</sub> and 53.2 eV for Se 3d<sub>5/2</sub> (Figure 1i). The XPS spectrum of O1s shown in Figure 1j is fitted at 532 and

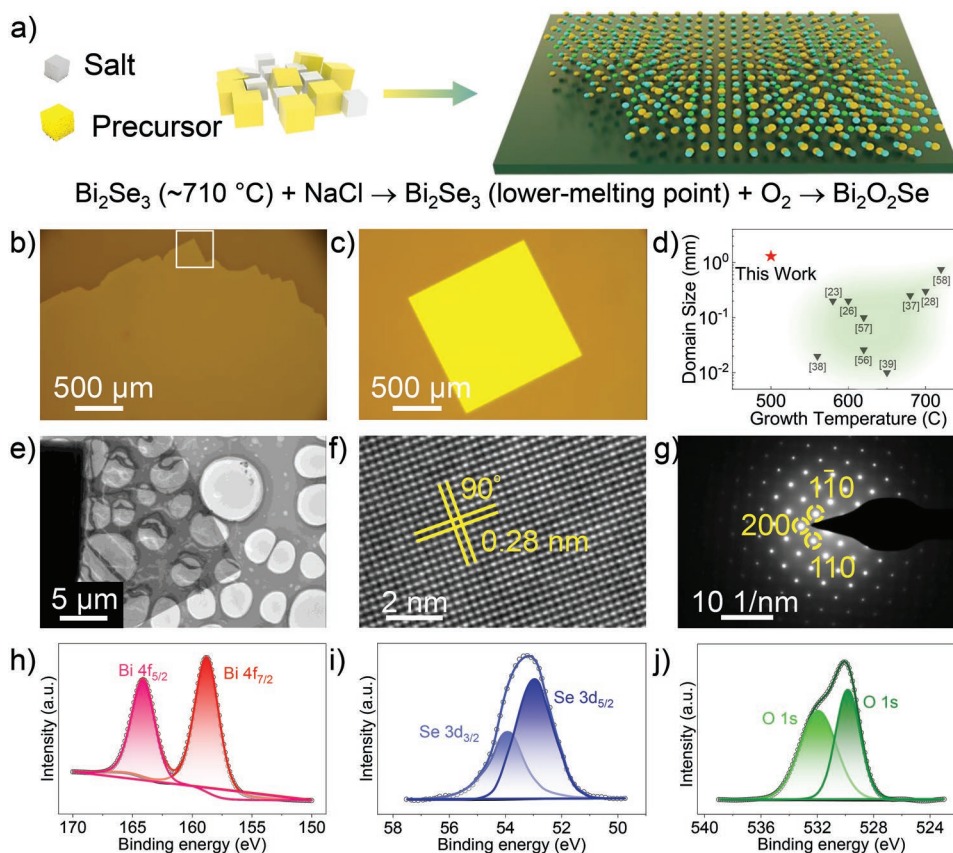


**Figure 1.** Salt-assisted low-temperature CVD growth of 2D  $\text{Bi}_2\text{O}_2\text{Se}$  single crystals. a) Schematic illustration for salt-assisted large-scale growth of 2D  $\text{Bi}_2\text{O}_2\text{Se}$  nanosheets on f-mica at low temperature of  $500^\circ\text{C}$ . b) A typical optical microscope image of  $\text{Bi}_2\text{O}_2\text{Se}$  nanosheet with an average size of more than 3 mm. c) An optical microscope image of another large-domain single crystal 2D  $\text{Bi}_2\text{O}_2\text{Se}$  with a size  $> 1.3$  mm. d) Domain sizes of single crystal 2D  $\text{Bi}_2\text{O}_2\text{Se}$  flakes reported in the literature. e) The TEM morphology of 2D  $\text{Bi}_2\text{O}_2\text{Se}$  nanosheet on a copper grid. f) HRTEM image of the salt-assisted CVD synthesized 2D  $\text{Bi}_2\text{O}_2\text{Se}$  representing a lattice spacing of 2.8 Å for (110). g) The single crystalline feature of a 2D  $\text{Bi}_2\text{O}_2\text{Se}$  nanosheet is exhibited in the SAED pattern. h–j) The elemental compositions of Bi, Se and O in the 2D  $\text{Bi}_2\text{O}_2\text{Se}$  nanosheet are shown in the XPS spectra.

529.9 eV. It is identified that the binding energy of all the peaks is consistent with the elemental composition of  $\text{Bi}_2\text{O}_2\text{Se}$ . Further, the quantitative examination specifies Se to Bi atomic ratio of 1:2, identifying the formation of  $\text{Bi}_2\text{O}_2\text{Se}$  flakes with adequate stoichiometry. Furthermore, high annular dark field (HAADF) scanning TEM (STEM) micrographs with relative elemental mapping shown in Figure S6 (Supporting Information) confirm a homogeneous distribution of Bi, Se, and O elements. Therefore, the salt-assisted CVD-grown 2D  $\text{Bi}_2\text{O}_2\text{Se}$  nanosheets represent good homogeneity, high crystal quality, and stoichiometry and indicate excellent consistency with prior reports.<sup>[25,27–30]</sup>

Raman spectroscopy is an analytical non-destructive, and fast technique to investigate structural and chemical information of layer-dependent 2D materials by its characteristic Raman fingerprint. Herein, we have examined the Raman scattering of multilayer to monolayer  $\text{Bi}_2\text{O}_2\text{Se}$ . **Figure 2a** represents the AFM image of  $\text{Bi}_2\text{O}_2\text{Se}$ , and we analyzed that the thickness of the flake is  $\approx 0.8$  nm, close to the theoretical thickness of monolayer  $\text{Bi}_2\text{O}_2\text{Se}$  ( $\approx 0.61$  nm). The thicknesses of two layers (Figure 2b) and 18 layers (Figure 2c)  $\text{Bi}_2\text{O}_2\text{Se}$  flakes are 1.3 and 11 nm, respectively. This analysis confirms that salt-assisted CVD has the ability for the growth of 2D  $\text{Bi}_2\text{O}_2\text{Se}$  flakes with precise

control over the thickness of the material. Figure 2d displays the Raman spectra of the monolayer to 32 layers and bulk  $\text{Bi}_2\text{O}_2\text{Se}$  on the mica substrate, and the samples were excited by using a 532 nm laser. All the samples ranging from bulk to four-layered  $\text{Bi}_2\text{O}_2\text{Se}$  originate  $A_{1g}$  out-of-plane vibrational mode. However, the  $A_{1g}$  vibrational mode is too weak to be observed for monolayer, bilayer, and trilayer  $\text{Bi}_2\text{O}_2\text{Se}$  flakes. Importantly, we investigate that the  $A_{1g}$  vibrational mode is robust and sensitive to the layered numbers of  $\text{Bi}_2\text{O}_2\text{Se}$ . Moreover, the peak position of the  $A_{1g}$  vibrational mode represents a redshift of  $\approx 5.7$   $\text{cm}^{-1}$  from four layered ( $162.4$   $\text{cm}^{-1}$ ) to bulk ( $156.7$   $\text{cm}^{-1}$ )  $\text{Bi}_2\text{O}_2\text{Se}$  sample which can be observed in Figure 2e. Figure 2g indicates a Raman intensity mapping of  $A_{1g}$  peak ( $158$   $\text{cm}^{-1}$ ) of 9 layered  $\text{Bi}_2\text{O}_2\text{Se}$  flake shown in Figure 2f. The Raman map shows an excellent uniformity of the flake, which indicates that the color mapping is uniform throughout the surface. Salt-assisted grown  $\text{Bi}_2\text{O}_2\text{Se}$  has a similar quality and layer-dependent Raman spectroscopy reported by CVD-grown  $\text{Bi}_2\text{O}_2\text{Se}$ .<sup>[30]</sup>

The long-term stability and surface roughness of 2D materials in the air are imperative figures of merit for advanced manufacturing techniques. Thereby, we performed an imperial examination of the environmental stability of salt-assisted CVD-grown  $\text{Bi}_2\text{O}_2\text{Se}$ . In this procedure, we initially prepared

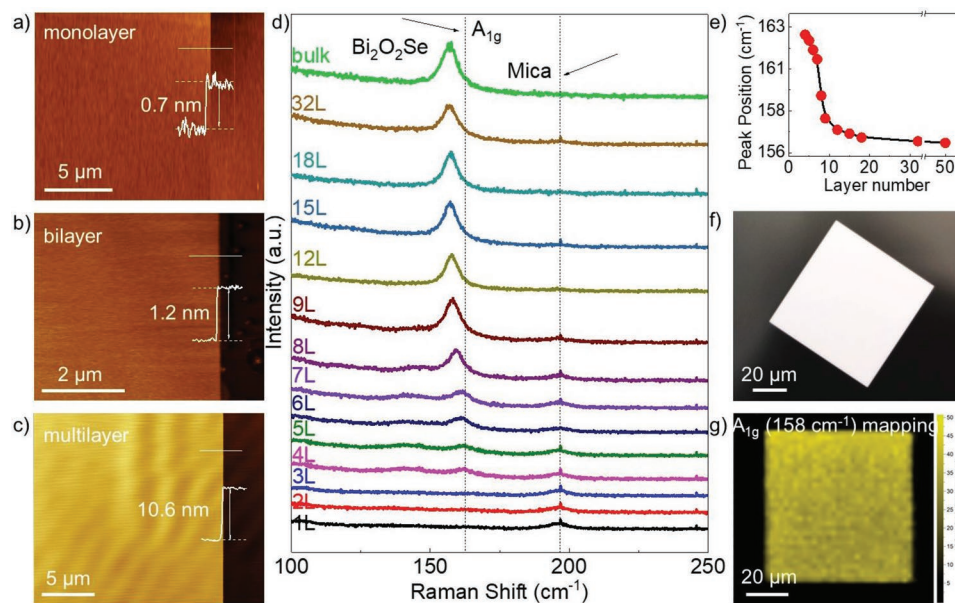


**Figure 2.** The characterization of the salt-assisted CVD growth of  $\text{Bi}_2\text{O}_2\text{Se}$  nanosheets on mica. a) AFM topography of a monolayer  $\text{Bi}_2\text{O}_2\text{Se}$  nanosheet with a thickness of 0.8 nm. b) AFM of a bilayer  $\text{Bi}_2\text{O}_2\text{Se}$  nanosheet with a thickness of 1.3 nm. c) AFM of a multilayer  $\text{Bi}_2\text{O}_2\text{Se}$  nanosheet with a thickness of 11 nm. d) Layer-dependent Raman spectra of salt-assisted CVD grown  $\text{Bi}_2\text{O}_2\text{Se}$  nanosheets, exhibiting a redshift in the out-plane vibrational mode from monolayer to bulk  $\text{Bi}_2\text{O}_2\text{Se}$  and is visible in (e). f,g) Optical micrograph image and Raman map of  $A_{1g}$  peak of a  $\text{Bi}_2\text{O}_2\text{Se}$  nanosheet represent an excellent uniformity.

2D  $\text{Bi}_2\text{O}_2\text{Se}$  flakes and then monitored the variation in surface roughness, thickness, and crystal quality by employing optical microscopy, AFM, and Raman spectroscopy. **Figure 3a–c** reveals the images of freshly grown  $\text{Bi}_2\text{O}_2\text{Se}$  flakes taken by optical microscope and the same nanoflakes after exposing the samples to air for 1 year and 1.5 years. It is evident by initial findings that  $\text{Bi}_2\text{O}_2\text{Se}$  flakes sustain their decency without conspicuous structural deformation. The topographical images of the air-exposed samples for 1 and 1.5 years represent similar thickness ( $\approx 2.4$  nm) as that of freshly grown  $\text{Bi}_2\text{O}_2\text{Se}$  flake (Figure 3d–f). In addition, the average surface roughness ( $R_a$ ) of the fresh flake is 0.6 nm, and for 1 year and 1.5 years, the exposed flake is 0.65 and 0.68 nm, which indicates that the air exposure does not greatly impact the surface of the flakes even after 1.5 years (Figure 3g). Therefore, the AFM analysis indicates that the samples remain clean and homogeneous, which designates the excellent stability of the samples in the ambient environment. The structural analysis of fresh and air-exposed  $\text{Bi}_2\text{O}_2\text{Se}$  flakes was further confirmed with Raman spectroscopy. It can be manifested from Raman spectra shown in Figure 3h that the peaks from the  $A_{1g}$  vibrational mode of samples before and after air exposure remain identical. Therefore, these results clearly demonstrate that 2D  $\text{Bi}_2\text{O}_2\text{Se}$  flakes remain stable in the environment, which is favorable for constructing electronic devices based on 2D materials.

Due to the accessibility of large-scale, high-quality salt-assisted CVD-grown  $\text{Bi}_2\text{O}_2\text{Se}$  flakes, we fabricated  $\text{Bi}_2\text{O}_2\text{Se}$ -based FET to study their electrical performance. The samples were transferred onto a  $\text{SiO}_2/\text{Si}$  substrate for the back gate terminal of FET. The procedure for transferring 2D  $\text{Bi}_2\text{O}_2\text{Se}$  is shown in our previous study.<sup>[30]</sup> The pattern for source and drain terminals of FET was designed by an electron beam

lithography technique. The metallic electrodes were made of gold and chromium (100 nm of Au on 5 nm of Cr) by e-beam evaporation (see details in the experimental section). The scheme for the construction of  $\text{Bi}_2\text{O}_2\text{Se}$ -based FET is represented in **Figure 4a**. The optical microscope image of  $\text{Bi}_2\text{O}_2\text{Se}$ -based FET with channel length ( $L$ ) of  $\approx 80.6$   $\mu\text{m}$  and channel width ( $W$ ) of  $\approx 45.6$   $\mu\text{m}$  is presented in the inset of **Figure 4b**. The room temperature output curves ( $I_D-V_D$ ) are demonstrated in **Figure 4b**. The back gate voltage ( $V_G$ ) of the device is modulated from  $-5$  to  $10$  V with a step voltage of 2 V. It is evident from the output characteristic curves that the drain current ( $I_D$ ) is greatly dependent on the applied  $V_G$ , which indicates back gate controllability of FET. The symmetric and linear  $I_D-V_D$  curves demonstrate excellent contact between  $\text{Bi}_2\text{O}_2\text{Se}$  and electrodes.<sup>[25]</sup> These curves reveal a typical  $n$ -type semiconducting nature by which  $I_D$  increases with a rise in positive  $V_G$ . The current ratio between  $V_G$  of  $-5$  and  $10$  V is  $\approx 10^7$ , indicated by a semi-log scale curve plotted in **Figure S7** (Supporting Information). The transfer curves ( $I_D-V_G$ ) in linear and logarithmic scales at constant  $V_D = 1$  V are represented in **Figure 4c**. These plots investigate the rise in  $I_D$  as a function of  $V_G$ , which provides another justification for the  $n$ -type conductivity of  $\text{Bi}_2\text{O}_2\text{Se}$ -based FET. The extracted field-effect mobility ( $\mu$ ) from these curves is  $\approx 287$   $\text{cm}^2 \text{V}^{-1} \text{s}^{-1}$ , and the corresponding carrier concentration ( $n$ ) is  $3.3 \times 10^{11} \text{cm}^{-2}$  at  $V_D = 1$  V. The extracted value of threshold voltage by extrapolation of the transfer curve in the linear region is  $-1.9$  V. **Figure 4d,e** provides  $I_D-V_G$  plot in a linear and logarithmic scales as a variable of  $V_D$  that further confirms the  $n$ -type nature of  $\text{Bi}_2\text{O}_2\text{Se}$  based FET device. **Figure 4f** presents another figure of the merit of FET which is  $I_{\text{on}}/I_{\text{off}}$  and it can be observed that the fabricated device provides a decent value that is  $10^7$ . Therefore, salt-assisted CVD growth

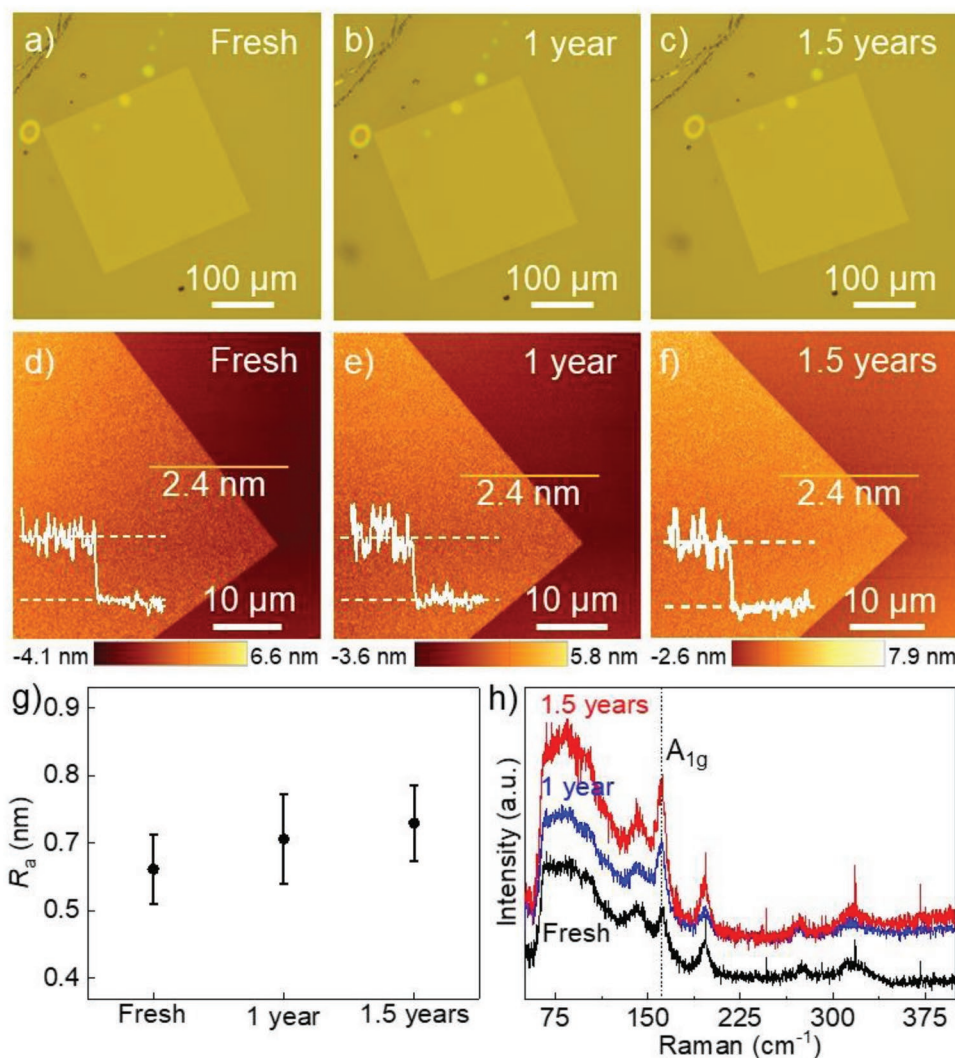


**Figure 3.** Environmental stability of atomically thin Bi<sub>2</sub>O<sub>2</sub>Se nanosheets. a–c) Optical microscope and d–f) AFM images of freshly synthesized nanosheet after air exposure of 1 year and 1.5 years, respectively. g) Arithmetic mean roughness ( $R_a$ ) of freshly grown Bi<sub>2</sub>O<sub>2</sub>Se nanosheets and air-exposed samples. h) Raman spectroscopy of freshly synthesized 2D Bi<sub>2</sub>O<sub>2</sub>Se nanosheets and after air exposure of 1 and 1.5 years.

of Bi<sub>2</sub>O<sub>2</sub>Se provides a high crystal quality and is a suitable candidate for high-performance electronics.

### 3. Conclusion

We have developed a salt-assisted CVD technique to grow 2D single crystal Bi<sub>2</sub>O<sub>2</sub>Se with monolayer to multilayer thickness at a low temperature of 500 °C. The materials reveal high crystal quality, good stoichiometry, and excellent stability even after air exposure for 1.5 years. We investigated that the A<sub>1g</sub> vibrational mode of four layered salt-assisted grown Bi<sub>2</sub>O<sub>2</sub>Se scatters a Raman peak at 162.4 cm<sup>-1</sup>. Later, an obvious redshift of ≈5.7 cm<sup>-1</sup> is recorded with an increase in the thickness of Bi<sub>2</sub>O<sub>2</sub>Se flakes. Moreover, the 2.4 nm thick Bi<sub>2</sub>O<sub>2</sub>Se manifests excellent fresh and 1.5 years of air-exposed sample stability. The backgated Bi<sub>2</sub>O<sub>2</sub>Se-based FET indicates n-type semiconducting features with a high current on/off ratio > 10<sup>7</sup>, decent carrier mobility of ≈287 cm<sup>2</sup> V<sup>-1</sup> s<sup>-1</sup>, and a carrier concentration of

3.3 × 10<sup>11</sup> cm<sup>-2</sup>. Considering the high crystal quality and excellent air stability of salt-assisted CVD-grown Bi<sub>2</sub>O<sub>2</sub>Se for FETs, this work demonstrates the potential of 2D material for future state-of-the-art electronic devices.

### 4. Experimental Section

**Salt-Assisted CVD Growth of Bi<sub>2</sub>O<sub>2</sub>Se on *f*-Mica:** 2D Bi<sub>2</sub>O<sub>2</sub>Se was grown on the *f*-mica substrate using a salt-assisted CVD technique. In this process, Bi<sub>2</sub>Se<sub>3</sub> and NaCl were located in the tube's hot center furnace. Several 1 × 1 cm<sup>2</sup> mica pieces were located 14 cm downstream from the tube center to grow the Bi<sub>2</sub>O<sub>2</sub>Se flakes. Initially, oxygen and other impurity gases were exhausted by Ar gas flushed into the tube furnace for 10 min. During the growth procedure, the central zone was heated to 500 °C, and the growth temperature for Bi<sub>2</sub>O<sub>2</sub>Se was fixed at 500 °C for 30 min. Note that this growth temperature is lower than other reports in growing 2D Bi<sub>2</sub>O<sub>2</sub>Se.<sup>[25,28,39]</sup> Simultaneously, a mixture of O<sub>2</sub> (10 sccm) and Ar gases (190 sccm) was passed through the tube furnace, and pressure was maintained between 350–400 Torr. Importantly, the amount of O<sub>2</sub> gas played a critical role in the successful deposition of Bi<sub>2</sub>O<sub>2</sub>Se

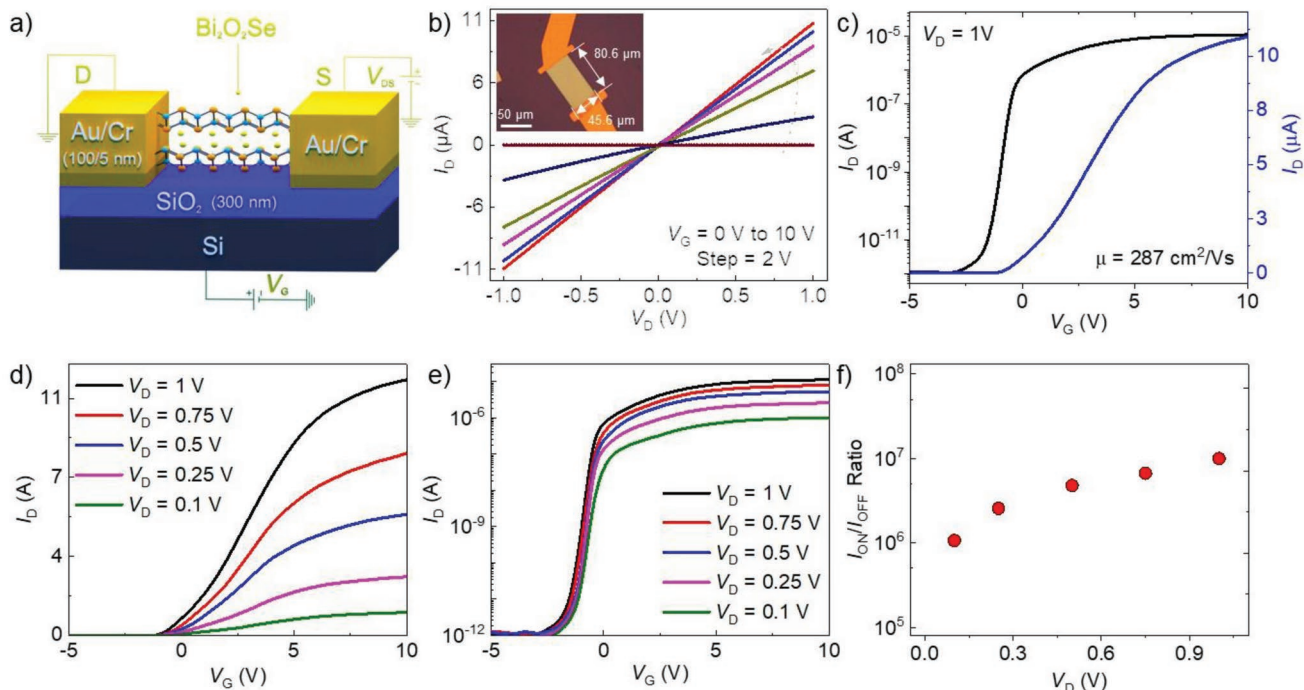


**Figure 4.** The electrical performance of  $\text{Bi}_2\text{O}_2\text{Se}$ -based FET device. a) Schematic design of backgated  $\text{Bi}_2\text{O}_2\text{Se}$  nanosheet-based FET. b) The inset of the figure represents the typical optical microscopic image of  $\text{Bi}_2\text{O}_2\text{Se}$  nanosheet-based FET with a width ( $W$ ) and channel length of 45.6 and 80.6  $\mu\text{m}$ , respectively, whereas the output curves ( $I_D$ - $V_D$ ) as a function of gate voltage ( $V_G$ ) are shown in the main figure. c) The transfer curves ( $I_D$ - $V_G$ ) of the device in linear and logarithmic scale at  $V_D$  of 5 V. d) The transfer family curves of the FET device as a function of  $V_D$  are represented in linear scale, whereas e) depicts these curves in logarithmic scale. f) The current on/off ratio of the device as a function of  $V_D$  represents a maximum value of  $10^7$ .

nanosheets. Finally, the system's temperature was cooled down naturally to avoid structural deformation of the grown nanosheets.

**Characterization:** The morphology of synthesized  $\text{Bi}_2\text{O}_2\text{Se}$  nanosheets was identified with the help of an optical microscope (SOPTOP CX40M). The topographical analyses, such as the thickness and roughness of the samples, were investigated by AFM (PSIA XE-100E). The crystal structure of  $\text{Bi}_2\text{O}_2\text{Se}$  nanosheets was initially elucidated by XRD using  $\text{Cu K}\alpha$  radiation with wavelength  $\lambda = 0.15418 \text{ nm}$  (ARL XTRA). Later, the chemical composition of the samples was ensured using XPS (Thermo Scientific ESCALAB Xi+). Next, a detailed morphology and crystal structure were analyzed by using TEM (FEI Talos F200S). The Raman spectroscopy analysis and mapping were achieved using a 532 nm laser (Horiba LabRAB).

**Transfer of 2D  $\text{Bi}_2\text{O}_2\text{Se}$  Nanosheets:** For device fabrication, 2D  $\text{Bi}_2\text{O}_2\text{Se}$  nanosheets were transferred on  $\text{SiO}_2/\text{Si}$  substrate by polydimethylsiloxane (PDMS) and polymethyl methacrylate (PMMA) assisted method. Briefly, a thin layer of PMMA (1200 rpm) was first coated on  $\text{Bi}_2\text{O}_2\text{Se}/\text{mica}$  for 120 s. The deposited polymer layer was then dried in the air using a heat treatment at 150  $^\circ\text{C}$  for 60 s. Later, a commercially purchased PDMS sheet was attached on PMMA/ $\text{Bi}_2\text{O}_2\text{Se}/\text{mica}$  to support the polymer layer. The adhesion between the tethered PDMS and polymer was significantly advanced by gradually heating PDMS/PMMA/ $\text{Bi}_2\text{O}_2\text{Se}/\text{mica}$  at 70  $^\circ\text{C}$  for 120 s. The PDMS/PMMA/ $\text{Bi}_2\text{O}_2\text{Se}$  was peeled off from mica due to the hydrophilic nature of mica in  $\text{H}_2\text{O}$  compared to the hydrophobic nature of PMMA. Later, the sample was dried at 70  $^\circ\text{C}$  in air for 120 s. Next, PDMS/PMMA/ $\text{Bi}_2\text{O}_2\text{Se}$  layer was attached to the  $\text{SiO}_2/\text{Si}$  substrate, followed by the gentle removal of PDMS mechanically by heating the sample at 120  $^\circ\text{C}$ . In the final step, the polymer was removed with acetone and cleaned the sample with water and isopropyl alcohol.

**Device Fabrication and Measurements:** To manufacture backgated FET,  $\text{Bi}_2\text{O}_2\text{Se}$  nanosheets were transferred onto  $\text{SiO}_2/\text{Si}$ , and the thickness of the oxide layer was 300 nm. Initially, a standard photolithography procedure was adopted to define the alignment markers. Then, the device electrodes were designed by the standard EBL process. Briefly, a polymer

layer of PMMA was coated on  $\text{Bi}_2\text{O}_2\text{Se}/\text{SiO}_2/\text{Si}$  in the beginning. Later, the source and drain patterns were defined by EBL. After the electrode pattern was developed in methyl isobutyl ketone/IPA, source and drain electrodes were deposited using an electron beam evaporation made by gold/chromium (Au/Cr, 100 nm/5 nm). After a lift-off procedure, the devices were annealed at 150  $^\circ\text{C}$  in a vacuum (under an Ar pressure of 300 Torr) for 2 h to remove photoresist residues and improve the quality of the contact. The  $\text{Bi}_2\text{O}_2\text{Se}$ -based FET performance was estimated by Keithley 4200 semiconductor property analyzer. The FET figure of merits, such as field effect mobility, carrier concentration, and threshold voltage, were extracted from the transfer characteristic curves. Specifically, the field-effect mobility of  $\text{Bi}_2\text{O}_2\text{Se}$ -based-FET was analyzed by extrapolating of transfer curve and by using the expression  $\mu = L/WC_iV_D \times dI_D/dV_G$ . The capacitance per unit area ( $C_i$ ) was calculated by  $C_i = \epsilon_r\epsilon_0/d$ ; where  $\epsilon_r$  is the relative permittivity of  $\text{SiO}_2$ , and its value was 3.9,  $\epsilon_0$  is the permittivity of free space ( $8.85 \times 10^{-12} \text{ F m}^{-1}$ ), and  $d$  is the thickness of the oxide layer (300 nm). The charge carrier concentration of the device was extracted by  $n = I_dL/qWV_d\mu$ ; where  $q$  is the charge of an electron. The threshold voltage value was calculated by the intercept of the linear extrapolation of the transfer curve at the maximum slope.

## Supporting Information

Supporting Information is available from the Wiley Online Library or from the author.

## Acknowledgements

The authors acknowledge support by the National Natural Science Foundation of China (reference no. 2221101208) and the Science Foundation of Zhejiang Sc-Tech University (ZSTU).

## Conflict of Interest

The authors declare no conflict of interest.

## Data Availability Statement

The data that support the findings of this study are available from the corresponding author upon reasonable request.

## Keywords

2D materials, salt-assisted chemical vapor deposition (CVD), millimeter-size single crystals, Bi<sub>2</sub>O<sub>2</sub>Se, field-effect transistors, stability

Received: October 28, 2022

Revised: December 7, 2022

Published online: December 20, 2022

- [1] S.-T. M. Akkanen, H. A. Fernandez, Z. Sun, *Adv. Mater.* **2022**, *34*, 2110152.
- [2] C. Feng, Z.-P. Wu, K.-W. Huang, J. Ye, H. Zhang, *Adv. Mater.* **2022**, *34*, 2200180.
- [3] U. Khan, A. Nairan, J. Gao, Q. Zhang, *Small Structures* **2022**, 2200109.
- [4] X. Liu, M. S. Choi, E. Hwang, W. J. Yoo, J. Sun, *Adv. Mater.* **2022**, *34*, 2108425.
- [5] H.-F. Wang, C. Tang, C.-X. Zhao, J.-Q. Huang, Q. Zhang, *Adv. Funct. Mater.* **2022**, *32*, 2204755.
- [6] S. Wang, X. Liu, P. Zhou, *Adv. Mater.* **2022**, 2106886.
- [7] X. Xu, T. Guo, H. Kim, M. K. Hota, R. S. Alsaadi, M. Lanza, X. Zhang, H. N. Alshareef, *Adv. Mater.* **2022**, *34*, 2108258.
- [8] L. Patra, R. Pandey, *Mater. Today Commun.* **2022**, *31*, 103623.
- [9] Y. Liu, Y. Fang, D. Yang, X. Pi, P. Wang, *J. Phys.: Condens. Matter* **2022**, *34*, 183001.
- [10] S. Jana, A. Bandyopadhyay, S. Datta, D. Bhattacharya, D. Jana, *J. Phys.: Condens. Matter* **2021**, *34*, 053001.
- [11] W. Chen, U. Khan, S. Feng, B. Ding, X. Xu, B. Liu, *Adv. Funct. Mater.* **2020**, *30*, 2004960.
- [12] Z. Wu, Y. Wang, G. Liu, X. Yang, T. Wei, H. Zhang, J. Zhou, J. Zhu, *Mater. Today Energy* **2021**, *21*, 100810.
- [13] J. Yu, Q. Sun, *Appl. Phys. Lett.* **2018**, *112*, 053901.
- [14] Q. Zhang, X. Xiao, L. Li, D. Geng, W. Chen, W. Hu, *Small* **2022**, *18*, 2107241.
- [15] P. V. Pham, S. C. Bodepudi, K. Shehzad, Y. Liu, Y. Xu, B. Yu, X. Duan, *Chem. Rev.* **2022**, *122*, 6514.
- [16] S. Batool, M. Idrees, S.-R. Zhang, S.-T. Han, Y. Zhou, *Nanoscale Horiz.* **2022**, *7*, 480.
- [17] H. Xu, B. Ding, Y. Xu, Z. Huang, D. Wei, S. Chen, T. Lan, Y. Pan, H.-M. Cheng, B. Liu, *Nat. Nanotechnol.* **2022**, *17*, 1091.
- [18] Z. Huang, T. Lan, L. Dai, X. Zhao, Z. Wang, Z. Zhang, B. Li, J. Li, J. Liu, B. Ding, A. K. Geim, H.-M. Cheng, B. Liu, *Adv. Mater.* **2022**, *34*, 2110464.
- [19] M. Saeed, P. Palacios, M.-D. Wei, E. Baskent, C.-Y. Fan, B. Uzlu, K.-T. Wang, A. Hemmetter, Z. Wang, D. Neumaier, M. C. Lemme, R. Negra, *Adv. Mater.* **2022**, 2108473.
- [20] S. Thurakkal, X. Zhang, *Adv. Sci.* **2020**, *7*, 1902359.
- [21] S. Miao, T. Liu, Y. Du, X. Zhou, J. Gao, Y. Xie, F. Shen, Y. Liu, Y. Cho, *Nanomaterials* **2022**, *12*, 2100.
- [22] M. Liu, S. Feng, Y. Hou, S. Zhao, L. Tang, J. Liu, F. Wang, B. Liu, *Mater. Today* **2020**, *36*, 91.
- [23] S. Ahmed, J. Yi, *Nano-Micro Lett.* **2017**, *9*, 50.
- [24] Z. Cai, Y. Lai, S. Zhao, R. Zhang, J. Tan, S. Feng, J. Zou, L. Tang, J. Lin, B. Liu, H.-M. Cheng, *Natl Sci Rev* **2020**, *8*, 1.
- [25] J. Wu, H. Yuan, M. Meng, C. Chen, Y. Sun, Z. Chen, W. Dang, C. Tan, Y. Liu, J. Yin, Y. Zhou, S. Huang, H. Q. Xu, Y. Cui, H. Y. Hwang, Z. Liu, Y. Chen, B. Yan, H. Peng, *Nat. Nanotechnol.* **2017**, *12*, 530.
- [26] H. Fu, J. Wu, H. Peng, B. Yan, *Phys. Rev. B* **2018**, *97*, 241203.
- [27] J. Wu, Y. Liu, Z. Tan, C. Tan, J. Yin, T. Li, T. Tu, H. Peng, *Adv. Mater.* **2017**, *29*, 1704060.
- [28] J. Wu, C. Tan, Z. Tan, Y. Liu, J. Yin, W. Dang, M. Wang, H. Peng, *Nano Lett.* **2017**, *17*, 3021.
- [29] U. Khan, L. Tang, B. Ding, L. Yuting, S. Feng, W. Chen, M. J. Khan, B. Liu, H.-M. Cheng, *Adv. Funct. Mater.* **2021**, *31*, 2101170.
- [30] U. Khan, Y. Luo, L. Tang, C. Teng, J. Liu, B. Liu, H.-M. Cheng, *Adv. Funct. Mater.* **2019**, *29*, 1807979.
- [31] R. U. R. Sagar, U. Khan, M. Galluzzi, S. Aslam, A. Nairan, T. Anwar, W. Ahmad, M. Zhang, T. Liang, *ACS Appl. Electron. Mater.* **2020**, *2*, 2123.
- [32] Y. Liang, Y. Chen, Y. Sun, S. Xu, J. Wu, C. Tan, X. Xu, H. Yuan, L. Yang, Y. Chen, P. Gao, J. Guo, H. Peng, *Adv. Mater.* **2019**, *31*, 1901964.
- [33] Y. Song, Z. Li, H. Li, S. Tang, G. Mu, L. Xu, W. Peng, D. Shen, Y. Chen, X. Xie, M. Jiang, *Nanotechnology* **2020**, *31*, 165704.
- [34] T. Ghosh, M. Samanta, A. Vasdev, K. Dolui, J. Ghatak, T. Das, G. Sheet, K. Biswas, *Nano Lett.* **2019**, *19*, 5703.
- [35] X. Tian, H. Luo, R. Wei, C. Zhu, Q. Guo, D. Yang, F. Wang, J. Li, J. Qiu, *Adv. Mater.* **2018**, *30*, 1801021.
- [36] X. Pang, Y. Zhao, X. Gao, G. Wang, H. Sun, J. Yin, J. Zhu, *Chin. Chem. Lett.* **2021**, *32*, 3099.
- [37] M.-Q. Li, L.-Y. Dang, G.-G. Wang, F. Li, M. Han, Z.-P. Wu, G.-Z. Li, Z. Liu, J.-C. Han, *Adv. Mater.* **2020**, *5*, 2000180.
- [38] P. Li, A. Han, C. Zhang, X. He, J. Zhang, D. Zheng, L. Cheng, L.-J. Li, G.-X. Miao, X.-X. Zhang, *ACS Nano* **2020**, *14*, 11319.
- [39] J. Wu, C. Qiu, H. Fu, S. Chen, C. Zhang, Z. Dou, C. Tan, T. Tu, T. Li, Y. Zhang, Z. Zhang, L.-M. Peng, P. Gao, B. Yan, H. Peng, *Nano Lett.* **2019**, *19*, 197.
- [40] C. Hong, Y. Tao, A. Nie, M. Zhang, N. Wang, R. Li, J. Huang, Y. Huang, X. Ren, Y. Cheng, X. Liu, *ACS Nano* **2020**, *14*, 16803.
- [41] J. Li, Z. Wang, Y. Wen, J. Chu, L. Yin, R. Cheng, L. Lei, P. He, C. Jiang, L. Feng, J. He, *Adv. Funct. Mater.* **2018**, *28*, 1706437.
- [42] S. Xu, H. Fu, Y. Tian, T. Deng, J. Cai, J. Wu, T. Tu, T. Li, C. Tan, Y. Liang, C. Zhang, Z. Liu, Z. Liu, Y. Chen, Y. Jiang, B. Yan, H. Peng, *Angew. Chem., Int. Ed.* **2020**, *59*, 17938.
- [43] Y. Chen, W. Ma, C. Tan, M. Luo, W. Zhou, N. Yao, H. Wang, L. Zhang, T. Xu, T. Tong, Y. Zhou, Y. Xu, C. Yu, C. Shan, H. Peng, F. Yue, P. Wang, Z. Huang, W. Hu, *Adv. Funct. Mater.* **2021**, *31*, 2009554.
- [44] N. Fechner, T.-P. Fellingner, M. Antonietti, *Adv. Mater.* **2013**, *25*, 75.
- [45] X. Jin, L. Gao, *J. Am. Ceram. Soc.* **2004**, *87*, 533.
- [46] J. H. Sung, H. Heo, S. Si, Y. H. Kim, H. R. Noh, K. Song, J. Kim, C.-S. Lee, S.-Y. Seo, D.-H. Kim, H. K. Kim, H. W. Yeom, T.-H. Kim, S.-Y. Choi, J. S. Kim, M.-H. Jo, *Nat. Nanotechnol.* **2017**, *12*, 1064.
- [47] K. Chen, Z. Chen, X. Wan, Z. Zheng, F. Xie, W. Chen, X. Gui, H. Chen, W. Xie, J. Xu, *Adv. Mater.* **2017**, *29*, 1700704.
- [48] Y. Huan, J. Shi, X. Zou, Y. Gong, C. Xie, Z. Yang, Z. Zhang, Y. Gao, Y. Shi, M. Li, P. Yang, S. Jiang, M. Hong, L. Gu, Q. Zhang, X. Yan, Y. Zhang, *J. Am. Chem. Soc.* **2019**, *141*, 18694.
- [49] H. Wang, X. Huang, J. Lin, J. Cui, Y. Chen, C. Zhu, F. Liu, Q. Zeng, J. Zhou, P. Yu, X. Wang, H. He, S. H. Tsang, W. Gao, K. Suenaga, F. Ma, C. Yang, L. Lu, T. Yu, E. H. T. Teo, G. Liu, Z. Liu, *Nat. Commun.* **2017**, *8*, 394.
- [50] S. Jiang, J. Yang, Y. Shi, J. Zhao, C. Xie, L. Zhao, J. Fu, P. Yang, Y. Huan, Q. Xie, H. Jiang, Q. Zhang, X. Wang, F. Su, Y. Zhang, *Nano Res.* **2020**, *13*, 667.
- [51] X. Liu, N. Fechner, M. Antonietti, *Chem. Soc. Rev.* **2013**, *42*, 8237.
- [52] J. Zhou, J. Lin, X. Huang, Y. Zhou, Y. Chen, J. Xia, H. Wang, Y. Xie, H. Yu, J. Lei, D. Wu, F. Liu, Q. Fu, Q. Zeng, C.-H. Hsu, C. Yang,

- L. Lu, T. Yu, Z. Shen, H. Lin, B. I. Yakobson, Q. Liu, K. Suenaga, G. Liu, Z. Liu, *Nature* **2018**, 556, 355.
- [53] L. Huang, Z. Hu, H. Jin, J. Wu, K. Liu, Z. Xu, J. Wan, H. Zhou, J. Duan, B. Hu, J. Zhou, *Adv. Funct. Mater.* **2020**, 30, 1908486.
- [54] S. M. Shinde, K. P. Dhakal, X. Chen, W. S. Yun, J. Lee, H. Kim, J.-H. Ahn, *NPG Asia Mater.* **2018**, 10, e468.
- [55] P. Yang, X. Zou, Z. Zhang, M. Hong, J. Shi, S. Chen, J. Shu, L. Zhao, S. Jiang, X. Zhou, Y. Huan, C. Xie, P. Gao, Q. Chen, Q. Zhang, Z. Liu, Y. Zhang, *Nat. Commun.* **2018**, 9, 979.
- [56] X. Hu, P. Huang, B. Jin, X. Zhang, H. Li, X. Zhou, T. Zhai, *J. Am. Chem. Soc.* **2018**, 140, 12909.
- [57] J. Buha, R. Gaspari, A. E. Del Rio Castillo, F. Bonaccorso, L. Manna, *Nano Lett.* **2016**, 16, 4217.
- [58] K. Mazumder, P. M. Shirage, *J. Alloys Compd.* **2021**, 888, 161492.
- [59] H. Yang, W. Chen, X. Zheng, D. Yang, Y. Hu, X. Zhang, X. Ye, Y. Zhang, T. Jiang, G. Peng, X. Zhang, R. Zhang, C. Deng, S. Qin, *Nanoscale Res. Lett.* **2019**, 14, 371.
- [60] Z. Wu, G. Liu, Y. Wang, X. Yang, T. Wei, Q. Wang, J. Liang, N. Xu, Z. Li, B. Zhu, H. Qi, Y. Deng, J. Zhu, *Adv. Funct. Mater.* **2019**, 29, 1906639.
- [61] Q. Fu, C. Zhu, X. Zhao, X. Wang, A. Chaturvedi, C. Zhu, X. Wang, Q. Zeng, J. Zhou, F. Liu, B. K. Tay, H. Zhang, S. J. Pennycook, Z. Liu, *Adv. Mater.* **2019**, 31, 1804945.
- [62] X. Yang, Q. Zhang, Y. Song, Y. Fan, Y. He, Z. Zhu, Z. Bai, Q. Luo, G. Wang, G. Peng, M. Zhu, S. Qin, K. Novoselov, *ACS Appl. Mater. Interfaces* **2021**, 13, 49153.